

Dynamical entanglement percolation with spatially correlated disorder

Lorenzo Cirigliano,^{1,*} Valentina Brosco,¹ Claudio Castellano,²
Simone Felicetti,² Laura Pilozzi,² and Bernard van Heck¹

¹*Dipartimento di Fisica Università La Sapienza, I-00185 Rome, Italy*

²*Istituto dei Sistemi Complessi (ISC-CNR), Via dei Taurini 19, I-00185 Rome, Italy*

(Dated: January 12, 2026)

The distribution of entanglement between the nodes of a quantum network plays a fundamental role in quantum information applications. In this work, we investigate the dynamics of a network of qubits where each edge corresponds to an independent two-qubit interaction. By applying tools from percolation theory, we study how entanglement dynamically spreads across the network. We show that the interplay between unitary evolution and spatially correlated disorder leads to a non-standard percolation phenomenology, significantly richer than uniform bond percolation and featuring hysteresis. A two-colour correlated bond percolation model, whose phase diagram is determined via numerical simulations and a mean-field theory, fully elucidates the physics behind this phenomenon.

I. INTRODUCTION

Quantum networks are at the basis of distributed quantum information protocols [1–3], enabling secure communication [4–6], distributed quantum computing [7, 8], enhanced quantum sensing [9], and clock synchronization [10]. Beside their relevance for quantum information applications, quantum networks are the ideal playground for modeling complex quantum devices and many-body systems [11, 12] and they can be utilized to represent the structure of complex quantum states [13–17] and to benchmark the performance and efficiency of quantum processors and simulators [18–20].

Analogous to classical networks, an essential property of quantum networks is their long-range structure and connectivity. In classical complex networks, connectivity is typically determined by the underlying topology and link formation mechanisms [21]. In quantum networks, instead, connectivity emerges from quantum correlations and can be engineered and controlled dynamically. To enable quantum information processing on large scales, it is therefore crucial to develop reliable methods for establishing and maintaining long-range quantum connectivity. This entails the ability to distribute entanglement between distant nodes [22, 23], to manipulate quantum coherence and other quantum resources [24, 25], and to generate multipartite entangled states such as Greenberger–Horne–Zeilinger (GHZ) and cluster states [26, 27].

Entanglement percolation models [28–34] address the problem of creating entanglement between distant nodes when maximally entangled pairs are probabilistically established between nodes with a singlet conversion probability p . In one-dimensional networks, the probability of sharing a singlet between two distant nodes decays exponentially with their separation [29]. In higher-dimensional structures, however, the number of possible connecting paths increases, giving rise to a percolation

phenomenon: above a critical value of p , a giant connected cluster emerges that spans a finite fraction of the network. Once a path of singlets links two nodes, entanglement swapping allows the creation of a maximally entangled state between the end nodes, *i.e.* two arbitrary nodes can be connected by a singlet whenever they belong to the same cluster. In large networks, this occurs with a probability that becomes independent of the inter-node distance and system size. As discussed in various works (see *e.g.* Ref.[34]) the problem then maps to a standard bond percolation [35]: when p exceeds a critical threshold, entanglement percolates through the network, enabling quantum correlations to be distributed over arbitrarily large distances.

More recent advances have added layers of realism and sophistication to this picture. They have for instance addressed path-based percolation where communication consumes resources [36–38], the importance of non-shortest paths in network resilience [39], entanglement distribution in complex network topologies [40, 41], and the effect of distributed quantum memories [42].

In all these approaches, entanglement spreads through the network by distributing entangled pairs among the nodes. This perspective is natural within the context of quantum communication [4, 5], for example in networks of optically linked stations. However, in many relevant cases such as Heisenberg spin chains [43–47], entanglement is not simply distributed, but instead generated and modified by direct interactions between qubits. In such cases, entanglement becomes a dynamical resource.

In this work, we combine concepts from quantum network theory and percolation to investigate the dynamics of entanglement percolation in such interaction-driven quantum networks with spatially correlated disorder. The model we consider can be viewed as a time-dependent, coherent extension of the static entanglement-percolation scenario studied in previous works [29, 31, 33]. The network is initialized in a product state at $t = 0$ and then undergoes unitary evolution under qubit–qubit couplings for a finite time, after which

* lorenzo.cirigliano@uniroma1.it

the interactions are switched off. We then analyze the probability of generating long-range entanglement within a percolation framework.

We show that this dynamical setting can present a variety of interesting phenomena, in particular when unitary evolution occurs under a disordered network Hamiltonian with spatially correlated parameters. In this case, the probability of establishing long-range entanglement in the network displays hysteresis as a function of time, so that the standard picture based on uniform bond percolation [29] can no longer be applied. Instead, we can understand phenomenology using a two-colour inhomogeneous bond percolation model [48–50] with spatial constraints. Given the simplicity of the underlying dynamics, these effects likely represent only a small part of the broader landscape that emerges when time-dependent processes are incorporated into the study of quantum networks.

The manuscript is structured as follows. In Sec. II we describe the model in detail and recall the necessary notions of percolation theory. In Sec. III, we warm up by considering the case of a dynamical network with disorder but without correlations. In particular, we demonstrate some universal results on the percolating state of the network at long times, which indicate that the uniform bond percolation picture remains essentially unaltered. In Sec. IV we introduce spatial correlations into the picture, and reveal via controlled numerical experiments that they induce hysteresis in the time evolution of the network. In Sec. V we describe the mapping to the two-colour bond percolation model, which provides a minimal setting to understand the occurrence of hysteresis.

II. A DYNAMICAL MODEL OF ENTANGLEMENT PERCOLATION

We consider a quantum network model with N nodes representing stations, each with a given number of qubits. We label nodes with upper case letters, A,B,C and denote as i_X the i -th physical qubit at node X , with $i_X = 1, 2, \dots, n_X$. We assume that every qubit is associated only to one edge, $\varepsilon_{i_X j_Y}^{XY}$, of the graph, representing dynamical connections between stations, i.e. a qubit i_X on node X interacting with a qubit j_Y placed on node Y , see Figure 1. This implies that, by construction, the number of qubits, n_X , in a station equals the degree of the corresponding node. The system's Hamiltonian has the form

$$H = \frac{1}{2} \sum_{X \neq Y} \sum_{i_X, j_Y} J_{i_X j_Y}^{XY} \sigma_x^{i_X} \otimes \sigma_x^{j_Y} \quad (1)$$

where the matrix J defines the connections between the nodes and $\sigma_x^{i_X}$ is a Pauli matrix acting on the state of the qubit i_X . At time $t = 0$ the system is initialized in a simple product state of the form

$$|\Psi_0\rangle = \prod_X \prod_{i_X} |s\rangle_{i_X}, \quad (2)$$

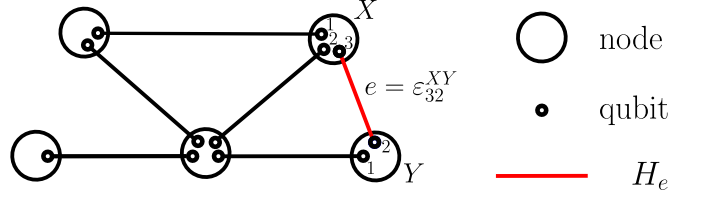


Figure 1. **Schematic representation of a quantum network.** We study a quantum network made of stations, forming the nodes of a graph, connected by edges that correspond to entangling interactions between pairs of qubits. Big circles denote stations, small circles represent qubits, lines indicate the presence of an interaction between two qubits. The interaction H_e between the qubits $i_X = 3$ and $j_Y = 2$, represented by the edge $e = \varepsilon_{i_X j_Y}^{XY}$, is highlighted in red. Note that each interaction involves two dedicated qubits, so that the number of qubits belonging to each station is equal to the degree of the corresponding node of the graph.

with $s = 0, 1$, where $|s\rangle_{i_X}$ denotes an eigenstate of $\sigma_z^{i_X}$. We choose the Hamiltonian (1) as a simple model that can generate entanglement acting on any initial state of the form (2).

Given the structure of the system's Hamiltonian defined by Eq. (1), to describe the time evolution of the network we label as $e \equiv \varepsilon_{i_X j_Y}^{XY}$ the generic element of the set \mathcal{E} of all edges of the network, one for each pair of nodes, and we introduce the entangling Hamiltonian H_e on the edge e as

$$H_e = \frac{1}{2} \omega_e \sigma_x^{i_X} \otimes \sigma_x^{j_Y}. \quad (3)$$

where ω_e is the value of $J_{i_X j_Y}^{XY}$ for the edge e . Note that in this notation, $H = \sum_{e \in \mathcal{E}} H_e$.

At time t , the state of the network can be expressed as a product of two-qubit states associated with each edge,

$$|\Psi(t)\rangle = \prod_{e \in \mathcal{E}} |\psi_e(t)\rangle, \quad (4)$$

with $|\psi_e(t)\rangle = e^{-iH_e t} |\psi_e(0)\rangle$, namely

$$|\psi_e(t)\rangle = \cos(\omega_e t/2) |s\rangle_{i_X} \otimes |s\rangle_{j_Y} - i \sin(\omega_e t/2) \sigma_x^{i_X} |s\rangle_{i_X} \otimes \sigma_x^{j_Y} |s\rangle_{j_Y}. \quad (5)$$

The quantum state of the network is a product two-qubit entangled states – one per edge e – each oscillating with frequency ω_e . Indeed, as discussed in Appendix A, applying the Schmidt decomposition to this two-qubit state yields

$$|\psi_e(t)\rangle = \sqrt{\lambda_e(t)} |x\rangle_{i_X} \otimes |x\rangle_{j_Y} + \sqrt{1 - \lambda_e(t)} |y\rangle_{i_X} \otimes |y\rangle_{j_Y}, \quad (6)$$

where $|x\rangle$ and $|y\rangle$ are some single-qubit states and the Schmidt coefficient λ_e is given by

$$\lambda_e(t) = \frac{1 + |\cos(\omega_e t)|}{2}. \quad (7)$$

Starting from this simple model of a dynamical quantum network, represented pictorially in Figure 2(a), our purpose is to study the likelihood to share entanglement between arbitrary distant qubits. Following Ref. [29], we assume that at a given time t it is possible to operate locally to attempt the conversion of $|\psi_e(t)\rangle$ into a maximally entangled state. The optimal conversion probability is [51]

$$\phi_e(t) = \min\{1, 2(1 - \lambda_e(t))\} = 1 - |\cos(\omega_e t)|. \quad (8)$$

After this operation has been carried out for each edge, one can use local entanglement swapping on maximally entangled adjacent edges in order to share entanglement among distant stations, provided that there is at least one path made of consecutive maximally entangled states connecting the corresponding nodes, see Figure 2(b).

Determining whether a maximally entangled path exists between two distant nodes is essentially equivalent to the study of connectivity properties of the network. From a percolation perspective, we say that each edge is *active* with probability $\phi_e(t)$ and we attempt to find a percolating path through the network.

Percolation theory offers guidance on the relevant quantities to study in order to characterise the entanglement of the network. The first such quantity is total fraction of maximally entangled states – in the percolation jargon, the fraction of active edges:

$$p(t) = \frac{1}{E} \sum_{e \in \mathcal{E}} \phi_e(t). \quad (9)$$

where E is the total number of edges in the network.

The second quantity, which we denote $P(t)$, is the fraction of nodes belonging to the largest component of nodes connected only via maximally-entangled states, see Figure 2(b). Note that $P(t)$ is related to the probability that long-distance entanglement can be shared among two nodes picked at random: in the large N limit, this probability is given by P^2 . When $P(t)$ scales with the size of the network N in the thermodynamic limit $N \rightarrow \infty$, we say that a giant component exists. In particular, if no giant component exists entanglement can be shared only locally. Even if the concept of giant component is formally well-defined only for $N \rightarrow \infty$, in practice the size of the largest connected component is a good proxy for it for finite N .

In percolation theory, the order parameter signalling that the network is in a percolating state is $P(p)$, that is the fraction of nodes belonging to the giant component as a function of the fraction of active edges [35]. In standard bond percolation with a fixed edge activation probability, P and p are static quantities and $P(p)$ is a well-defined single-valued function. We denote the order parameter of uniform bond percolation with $P_0(p)$. In contrast, we will see that in our dynamical model there may be multiple times along the time evolution characterized by the same $p(t)$ but by different $P(t)$. In this case, which occurs in the presence of correlations in the network parameters ω_e ,

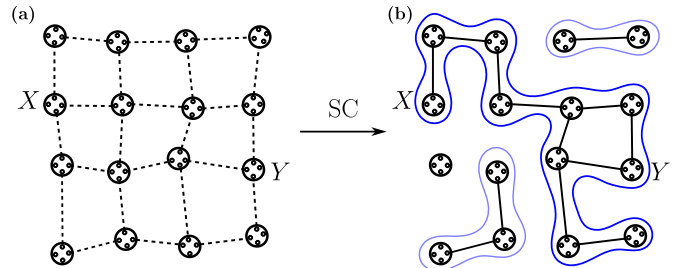


Figure 2. **Schematic representation of dynamical entanglement percolation.** (a) The dashed lines represent quantum states evolving as in Eq. (5). In this example, the network is a distortion of a square lattice, and spatial correlations are present between neighboring edges. (b) Result of the singlet conversion (SC) process. At a certain time t , each edge state $|\psi_e(t)\rangle$ is converted to a maximally entangled state with the singlet conversion probability $\phi_e(t)$ given in Eq. (8). Successful conversions are represented with continuous lines. The maximally entangled connected components are highlighted in blue, with thicker lines for the largest component (a proxy for giant component). The probability that X and Y can share entanglement is related to the size of the giant component. In this case, they both belong to the giant component.

$P(p)$ may become a multi-valued function which deviates from the order parameter P_0 .

III. EFFECT OF UNCORRELATED DISORDER

In this section, we explore the consequences of the dynamical evolution of the network under the assumption that the frequencies ω_e are uncorrelated. We begin by noticing that if the frequencies are all equal, i.e. $\omega_e = \Omega$ for all edges, we fall back to the classical entanglement percolation of Ref. [29], except with a time-dependent singlet-conversion probability $\phi_e(t) = 1 - |\cos(\Omega t)|$, uniform across the entire network. The fraction of active edges is therefore simply given by $p(t) = 1 - |\cos(\Omega t)|$, and the corresponding time evolution of $P(t)$ is also periodic in time, as shown in Fig. 3(a) for the case of a square lattice of nodes. The oscillations of $p(t)$ and $P(t)$ are always in phase, so the resulting curve $P(p)$ shown in Figure 3(e) is just the order parameter P_0 of bond percolation on a square lattice with uniform edge activation probability p [35], a single-valued function. The effect of the time evolution is only to move the state of the network back and forth along the curve $P_0(p)$ in a periodic fashion.

The situation becomes more interesting if we add some noise in the ω_e . If the frequencies are random variables distributed according to some distribution P_ω , for large networks we may estimate the fraction of active edges as

$$p(t) = 1 - \mathbb{E} [|\cos(\omega t)|] \quad (10)$$

where $\mathbb{E}[\cdot]$ denotes the expectation value under P_ω . In Appendix B, we show that for any continuous distribu-

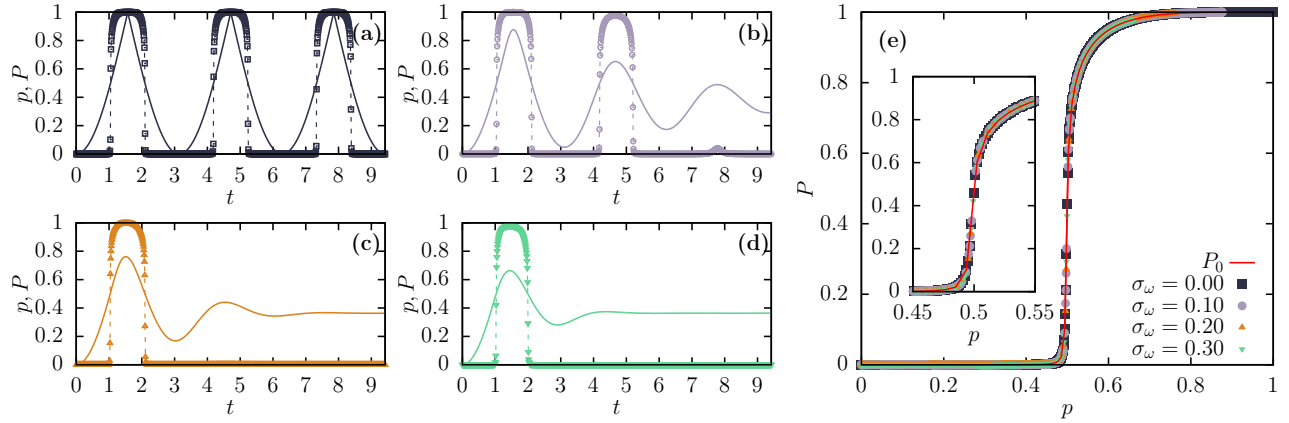


Figure 3. Dynamical entanglement percolation observables on two-dimensional square lattice with i.i.d. frequencies. (a)-(d) The observables $p(t)$ (solid lines) and $P(t)$ (symbols and dashed lines) for independent Gaussian frequencies with mean $\Omega = 1$ and (a) $\sigma_\omega = 0$ (uniform frequencies), (b) $\sigma_\omega = 0.1$, (c) $\sigma_\omega = 0.2$, (d) $\sigma_\omega = 0.3$. For uniform frequencies in panel (a), both p and P are periodic with period $T = \pi$. In all other cases, $p(t) \rightarrow p_\infty = 1 - 2/\pi$ for large times. (e) Parametric plot of $P(p)$ using the observables $p(t)$ and $P(t)$ in panels (a)-(d). The effect of the dynamical evolution disappears when observing the order parameter $P(p)$, as all curves are equivalent and they all reproduce uniform bond percolation $P_0(p)$ (red line). The role of t is just manifest in the fact that, depending on σ_ω , not all values of P can be reached. The inset in panel (e) shows the behavior of $P(p)$ close to the bond percolation threshold $p_c = 1/2$. All data perfectly overlap. For all plots, the system size is $L = 10^3$, hence $N = 10^6$. All results are averaged over 10 realizations of the disorder, and over 100 realizations of the edge activation process.

tion, at long times we reach a stationary state in which on average each edge is active with probability

$$p_\infty = 1 - \frac{2}{\pi} \approx 0.363. \quad (11)$$

This asymptotic result holds for any continuous probability density, as it is related to the large-argument behavior of the Fourier transform of P_ω , see Appendix B. The detailed shape of the distribution only determines the pre-asymptotic behaviour of $p(t)$.

A stable giant component exists at long times if p_∞ is larger than the standard bond percolation threshold p_c of the network. In turn, p_c depends on the topology of the interactions in the network. For example, for the triangular lattice $p_c = 2 \sin(\pi/18) \approx 0.347$ [35] and a giant component exists asymptotically. On the other hand, for the square lattice $p_c = 1/2$ [35], so long-distance entanglement cannot be established at long times. However, depending on the shape of the distribution, there may be intermediate times t such that $p(t) > p_c$, in which case a transient giant component occurs.

These results are corroborated numerically in Figure 3 for a square lattice with i.i.d. frequencies with a Gaussian distribution with average value Ω and standard deviation σ_ω . In this case, the asymptotic behavior is reached when $\sigma_\omega t \gg 1$. As seen in panels (a)-(d) of Fig. 3, for increasing values of σ_ω the oscillations in $p(t)$ saturate more quickly to the asymptotic value.

While in the disordered case the time evolution of p and P is not periodic anymore, their damped oscillations remain in phase as they did in the disorder-free case. The plot of P versus p in Fig. 3(e) shows a collapse over a sin-

gle curve, even when including data points from multiple oscillations and from different values of σ_ω .

In other words, although the system evolves dynamically in a way that depends on the disorder realization, at each time the values of $p(t)$ and $P(t)$ always fall on the curve $P_0(p)$ provided by the order parameter of uniform bond percolation. The network now performs damped oscillations back and forth along this curve and always ends up at the asymptotic point $P(p_\infty) = P_0(p_\infty)$. In the next Section, we show that the inclusion of spatial correlations in the network changes this picture qualitatively, introducing hysteresis.

IV. ADDING SPATIAL CORRELATIONS

Instead of considering independent random frequencies for different edges of the network, let us introduce correlation between frequencies of edges connected to the same node. A general way to do so is to first assign a weight g_X to each node X of the quantum network and assume that the frequency associated to the edge $\varepsilon_{i_X j_Y}^{XY}$ is a function of g_X and g_Y , i.e., $\omega_e = f(g_X, g_Y)$. Here f is a symmetric function of its two arguments, that we assume to be the same for every edge of the network. The dependence of the frequency ω_e on g_X and g_Y introduces correlations between frequencies of neighboring edges. The weight g_X may be related to physical properties of the station X , as for example its position and the nature of the connection with the other nodes.

Let us provide a practical instance of this procedure which is physically transparent and suitable for numeri-

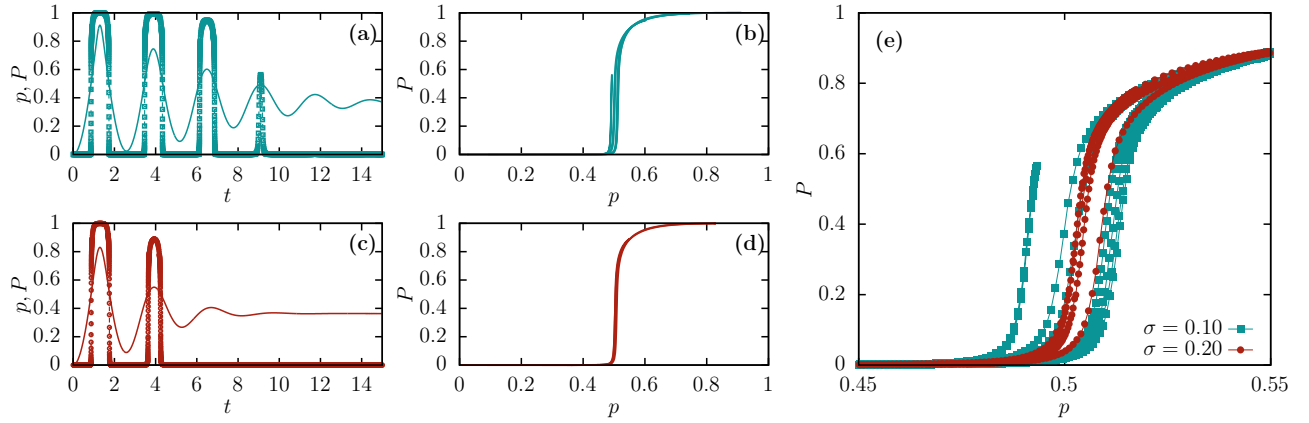


Figure 4. **Dynamical entanglement percolation observables on perturbed square lattice with exponentially decaying frequencies.** Results of numerical simulations on a perturbed square lattice with noise strength σ and frequencies depending on the distances as $\omega(d) = \Omega e^{-d/\lambda}$. We set $\Omega = 2$, $\lambda = 2$. (a) The observables $p(t)$ (solid lines) and $P(t)$ (symbols) for $\sigma = 0.1$, and (b) the corresponding parametric plot of $P(p)$. (c)-(d) As in (a)-(b) but for $\sigma = 0.2$. In both cases, the dynamics converges to the asymptotic value $p_\infty = 1 - 2/\pi$, after a preasymptotic oscillatory behavior which depends on the noise amplitude. (e) The behavior of the observables $P(p)$ as in panel (b) and (d) close to the uniform percolation threshold on the square lattice $p_c = 1/2$ [35]. In contrast to the case of independent random frequencies, P clearly depend on σ , and the order parameter $P(p)$ is no longer the same as uniform bond percolation.

cal study. We start with a two-dimensional square lattice of nodes with unit lattice spacing. We then randomly perturb the position of each node with a Gaussian noise $(\delta x, \delta y)$, where δx and δy are i.i.d. Gaussian variables with zero mean and variance σ^2 , see Figure 2(a). As a result, the distances $d_{ab} = |\vec{x}_a - \vec{x}_b|$ between the perturbed nodes of the lattice are correlated, in a way detailed in Appendix C. The frequency ω_e of an edge connecting nodes a and b is then chosen to be a deterministic function of the distance between the two nodes connected by that edge: $\omega_e \equiv \omega(d_{ab})$.

In Fig. 4 we report results of numerical simulations of the dynamical evolution of a network on the perturbed square lattice with frequencies that decay exponentially over a length scale λ , $\omega(d) = \Omega e^{-d/\lambda}$. As in the case without correlations, at long times $p(t)$ tends to $p_\infty = 1 - 2/\pi$, and the asymptotic limit is reached faster when disorder is stronger. Furthermore, as before, $P(t)$ becomes finite when $p(t)$ is large enough. However, in contrast to the case of i.i.d. frequencies, the $P(p)$ trajectory in panel (e) shows many branches: $P(t)$ has become a multi-valued function of $p(t)$. This hysteretic behavior is the manifest effect of local correlations in the frequencies induced by the spatial constraint.

The finite-time behavior in Fig. 4 depends on the specific choice of the function $\omega(d)$, which determines the frequency distribution of the network. In order to isolate the effect of correlations, we strip down our frequency assignment procedure to a threshold model in which ω_e can take one out of only two different values:

$$\omega_e = \begin{cases} \Omega_1 & \text{if } d_{ab} < \lambda, \\ \Omega_2 & \text{if } d_{ab} > \lambda. \end{cases} \quad (12)$$

Note that with no loss of generality we can set $\Omega_1 = 1$, or equivalently rescale t by Ω_1 , and use only one parameter $\tilde{\Omega} = \Omega_2/\Omega_1$. Because of the presence of the geometric constraint, the frequencies of edges having a common node are correlated. As shown in Appendix D, for the two-frequency model considered here, it is possible to fully characterize such correlations using only three probabilities which are determined by the model parameters σ and λ : (i) the probability η that $d_{ab} > \lambda$; (ii) the probability that two adjacent edges along the same direction are both shorter than λ ; (iii) the probability that two adjacent edges along orthogonal directions are both shorter than λ . As extensively discussed in Appendix D, for $\sigma < 0.5$ and $\lambda \approx 1$, the frequency distribution is balanced ($\eta \approx 1/2$): the number of edges with $\omega_e = \Omega_1$ and $\omega_e = \Omega_2$ is approximately the same. Furthermore, in this regime the frequencies are strongly anti-correlated along the same direction, either vertical or horizontal, and uncorrelated along orthogonal directions.

In Figure 5 we report the results of numerical simulations of this threshold model for some values of σ , $\tilde{\Omega}$, and $\lambda = 1$. To isolate the role played by correlations, for each simulation we run a parallel simulation in which, after fixing the realization of the disorder, we reshuffle the frequency and re-assign them to random edges. In this way we can compare two networks with exactly the same frequency distribution, but one with correlations and one without. In Fig. 5, we use the subscripts C and U on the observables to denote the correlated case and the uncorrelated case, respectively.

In either case, the frequency distribution is a discrete, a Bernoulli distribution. As shown in Appendix B, the

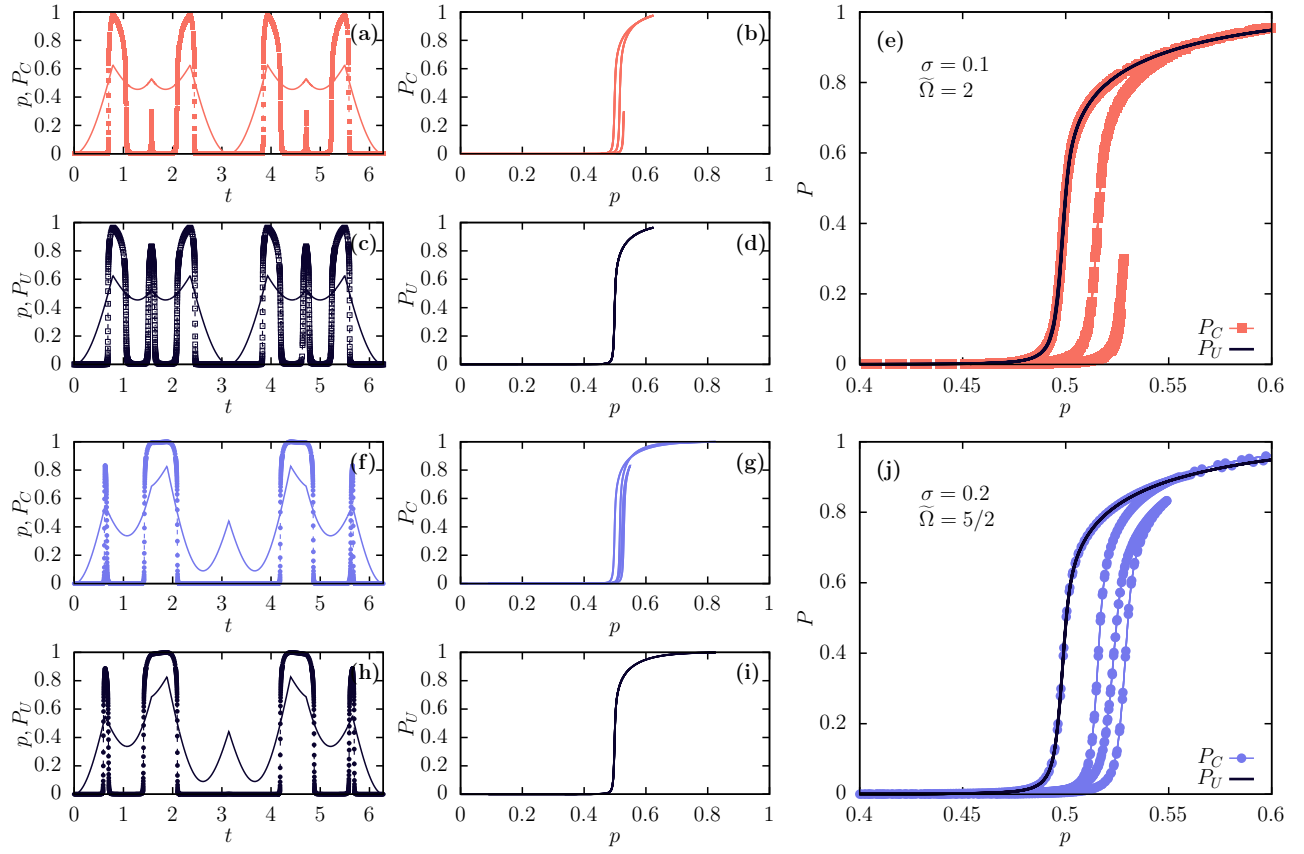


Figure 5. Dynamical entanglement percolation observables on perturbed square lattice with correlated Bernoulli frequencies. Results of numerical simulations on a perturbed square lattice with noise strength σ and frequencies depending on the distances as in Eq. (12). (a) The observables $p(t)$ (solid lines) and $P_C(t)$ (symbols and dashed lines) in the correlated case for $\sigma = 0.1$, $\tilde{\Omega} = 2$, $\lambda = 1$, and (b) the corresponding parametric plot of $P_C(p)$. (c)-(d) As in (a)-(b) but for the uncorrelated case. (e) The behavior of the observables $P_C(p)$ and $P_U(p)$ as in panel (b) and (d), respectively, close to the uniform percolation threshold on the square lattice $p_c = 1/2$ [35]. (f)-(j) as in (a)-(e) but for $\sigma = 0.2$, $\tilde{\Omega} = 5/2$, $\lambda = 1$. The comparison between the correlated and the uncorrelated scenario shows that the order parameters P_C clearly depend on the parameters σ and $\tilde{\Omega}$, exhibiting a nontrivial behavior with coexisting branches.

expected value of active edges is in this case

$$p(t) = 1 - \eta |\cos(\Omega_1 t)| - (1 - \eta) |\cos(\Omega_2 t)|. \quad (13)$$

It does not have an asymptotic value, but it undergoes periodic oscillations with a period which depends on the frequency ratio $\tilde{\Omega}$, and which becomes infinity if $\tilde{\Omega}$ is irrational. Importantly, the curve $p(t)$ does not depend on the presence of correlations between neighbouring edges.

The effect of correlation arises when inspecting $P(t)$. In the uncorrelated case, $P_U(t)$ follows the evolution of $p(t)$, and $P(p)$ is a well-defined function, as discussed in Sec. III. In the correlated case, instead, $P_C(t)$ shows the same type of multi-valued behavior already observed in Fig. 4 for a continuous distribution with correlations, see Fig. 5(e) and (j). The value of the order parameter at time t thus depends not only on the instantaneous value of p , but also on the previous history of the process $p(t)$, leading to hysteresis. Note also that $P_C(t)$ rises from zero at different values of $p(t)$ for different branches of the

hysteretic time evolution: in other words, the concept of a percolation threshold becomes blurred as there exists different thresholds. Note that if $\tilde{\Omega}$ is a rational number l/m with l, m coprimes, the time evolution is periodic with period $T = m\pi/\Omega_1$. In this case there is a finite set of percolation thresholds.

V. MAPPING TO TWO-COLOUR BOND PERCOLATION

The results in the previous section demonstrate that the dynamical entanglement percolation does not map to uniform bond percolation, because of the interplay between non-monotonic time evolution and correlated disorder. We now show that the more complex behavior is qualitatively captured by a two-colour inhomogeneous bond percolation model [48, 49, 52] with a specific type of spatial constraints. We assume that the edges of a reg-

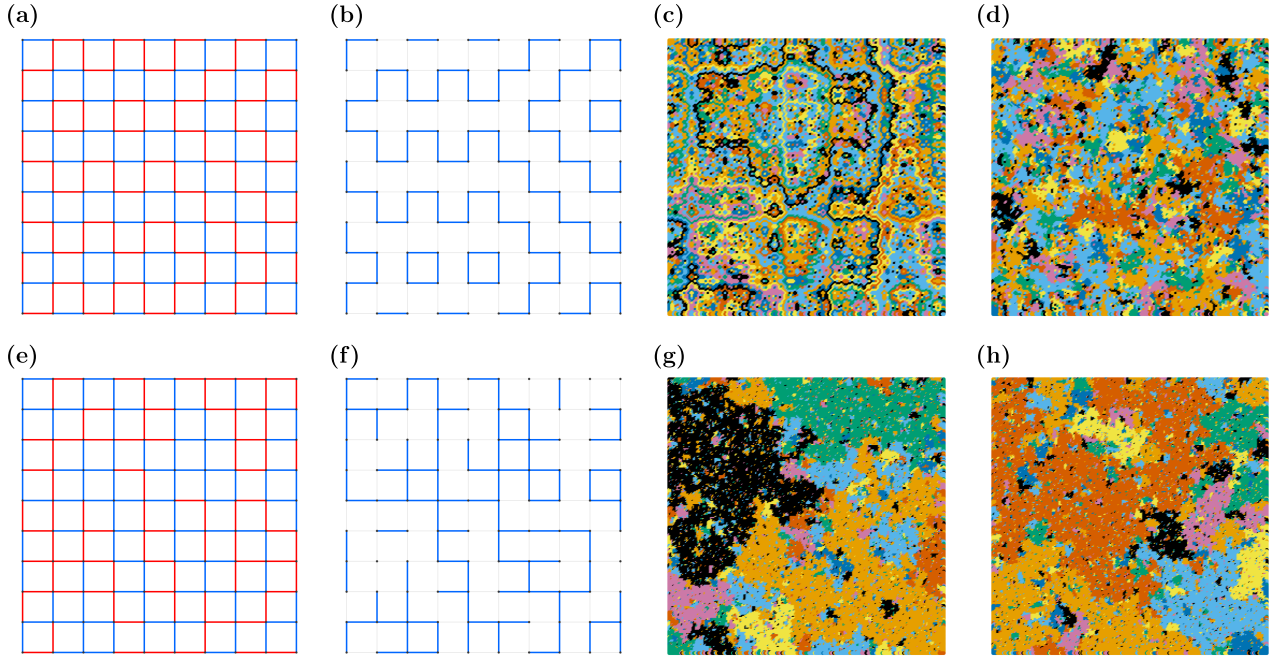


Figure 6. Two-colour bond percolation on a square lattice. (a) A configuration of the two-colour bond percolation model on a 10×10 square lattice. In (b) only blue edges are active, showing the presence of structural patterns. Snapshots of the connected components (coloured) on a 256×256 lattice for $p = 0.5$, using (c) $\phi_1 = 0, \phi_2 = 1$, and (d) $\phi_1 = 0.1, \phi_2 = 0.9$. Even if the fraction of active edges is the same, the two configurations are markedly distinct because of the strong spatial constraints. Panels (e)-(h) are as in (a)-(d) but for a random placement of the two colours, without the local constraints. The configurations in (g) and (h) are statistically equivalent.

ular square lattice of two colours, say red and blue. We also assume that half of edges is of type 1 (red) and it is active with probability ϕ_1 , and half is of type 2 (blue) active with probability ϕ_2 . The average fraction of active edges is $p = (\phi_1 + \phi_2)/2$, and for this model we denote the size of the giant component with $S(\phi_1, \phi_2)$. To mimic the spatial correlation patterns observed in perturbed lattices, we assume that along each direction edge colours are alternating, repeating a red/blue pattern, and that the colours of two adjacent orthogonal edges are independent. As shown in Fig. 6(a)-(b), this constraint leads to large-scale structural patterns. These are absent in samples where the red and blue edges occur with the same proportions but in randomly re-shuffled positions, as shown in Fig. 6(e)-(f).

Whether or not S can be expressed in terms of p corresponds to asking whether or not the curves $\phi_1 + \phi_2 = 2p$ are contour levels of S . If that is the case, we can write $P(p) = S(\phi_1, 2p - \phi_1)$ and the dependence on ϕ_1 cancels by definition. We expect that the spatial constraints producing the alternating pattern in the bond colors affect the behavior of the order parameter. For instance, Figure 6(c) and (d) show two configurations on the same two-colour lattice and for the same average fraction of active edges $p = 1/2$ but for (c) $\phi_1 = 0, \phi_2 = 1$, and (d) $\phi_1 = 0.1, \phi_2 = 0.9$. The presence of visually different spatial patterns for the same value of p indicates that

the cluster configurations also depend on which edges are active, not only on how many edges are active. This effect is not present instead if one considers a randomized placement of the two colours, as shown in Figure 6(e)-(h).

We determine the phase diagram $S(\phi_1, \phi_2)$ by means of extensive numerical simulations on large lattices, both for the alternating pattern and for the randomly reshuffled lattice. Results are presented in Figure 7(a). The closer to the percolating line, the more visible is the effect of the spatial constraints: the white dashed line bounds the region where $|S_U - S_C| > 10^{-2}$.

It is straightforward at this point to understand what is the role of the dynamics. Edge activation probabilities changing in time can be represented by a curve $\gamma(t) = (\phi_1(t), \phi_2(t))$ in the parameter space, see for instance the two lines in Figure 7(a) corresponding to time evolutions of the form

$$\phi_1(t) = 1 - |\cos(t)|, \quad \phi_2(t) = 1 - |\cos(\tilde{\Omega}t)|, \quad (14)$$

with $\tilde{\Omega} = 2$ (violet) and $\tilde{\Omega} = 5/2$ (green). Note that this choice of $\gamma(t)$ is meant to mimic the SCP given in Eq. (8). However, any function $\gamma : \mathbb{R} \rightarrow [0, 1] \times [0, 1]$ can be used to model the time evolution of ϕ_1 and ϕ_2 . The order parameter $P(t)$ is obtained by moving on the surface S along the curve γ , that is $P(t) = S(\gamma(t))$, see Figure 7(b). Finally, the order parameter $P(p)$ is plotted in Figure 7(c) and (d), and it clearly shows the same hysteretic behavior

observed for the case of dynamical entanglement percolation in perturbed lattices. Such a multi-branch behavior is the combined effect of (i) non-monotonic dynamical evolution of the edge activation probabilities, and (ii) strong spatial constraints.

Remarkably, for both $\tilde{\Omega} = 2$ and $\tilde{\Omega} = 5/2$ there exists one branch of P_C that overlaps with the order parameter P_U of uniform bond percolation. This happens because both curves pass through the point $\phi_1 = \phi_2 = 1/2$, where the distinction between the two colors disappear and the alternating pattern does not play any role. Close to this point, as one can see from the white dashed lines in Figure 7(a), the two order parameters are almost equal¹.

Finally, to prove that this hysteretic behavior is a truly thermodynamic effect that does not disappear in the infinite-size limit, in Appendix E we derive the mean-field solution for the two-colour bond percolation model, recovering a scenario qualitatively equivalent to what we observe here.

VI. DISCUSSION

Entanglement percolation [28–34] determines the minimum amount of entanglement required between nearest-neighbor nodes sharing an entangled qubit pair in order to establish a perfect long-distance quantum channel across a quantum network. Starting from the picture in which network nodes correspond to physical devices or stations hosting qubits, we extend the standard model of entanglement percolation to account for correlated singlet-conversion probabilities across edges connected to the same node. In particular, motivated by the observation that spatial constraints and other physical limitations shape the topology of quantum networks—similarly to the considerations in [6] for the optimization of quantum key-distribution networks—we introduce correlations that depend on the distance between nodes, going beyond the conventional independent-edge assumption. Furthermore, we consider scenarios in which entanglement between nodes is dynamically generated via a two-qubit interaction and oscillates in time due to the underlying Hamiltonian evolution. We analyse how this temporal behavior affects the emergence of long-range entanglement when oscillation frequencies vary locally across the network.

Our numerical and analytical study leads to the follow-

ing general findings. First, when the frequency distribution is continuous, the network evolves to a steady state in which edges become maximally entangled with probability $1 - 2/\pi$. Whether this corresponds to a percolating phase depends on the network topology. Second, when frequencies are uncorrelated, the percolation properties are accurately captured by the usual bond-percolation order parameter, in close analogy with the static case considered in previous works. Third, when frequencies are correlated, the network shows hysteretic behavior, oscillating in time between percolating and non-percolating phases. Finally, we show that a two-colour inhomogeneous bond-percolation model with spatial constraints provides a minimal theoretical framework capturing the key features of the correlated regime.

Our model is simple because the entanglement does not spread during the unitary evolution: the quantum state of the network is a simple tensor product of two-qubit states associated with each edge of the network. Nevertheless, the resulting behavior is rather complex from a percolation theory perspective, going qualitatively beyond that of standard entanglement percolation. A challenging and interesting task would be to study the effect of entanglement spreading during unitary evolution, e.g. through the action of local interaction terms at each node of the networks.

ACKNOWLEDGMENTS

This work was co-funded by Project PNRR MUR PE 0000023-NQSTI and Project PNRR MUR project CN 00000013-ICSC. C.C. acknowledges the PRIN project No. 20223W2JKJ “WECARE”, CUP B53D23003880006, financed by the Italian Ministry of University and Research (MUR), Piano Nazionale Di Ripresa e Resilienza (PNRR), Missione 4 “Istruzione e Ricerca” - Componente C2 Investimento 1.1, funded by the European Union - NextGenerationEU.

DATA AVAILABILITY

All the data generated for the numerical studies reported in this work can be reproduced using the code available at [53].

¹ One may wonder if this happens for any $\tilde{\Omega}$. Solving for τ the equation $\phi_1(\tau) = 1/2$ we get $\tau = k\pi \pm \pi/3$, with $k \in \mathbb{Z}$. Thus setting $\phi_2(\tau) = 1/2$ we obtain $\tilde{\Omega}\tau = q\pi \pm \pi/3$, with $q \in \mathbb{Z}$. Simplifying, we finally get

$$\tilde{\Omega} = \frac{3q \pm 1}{3k \pm 1}. \quad (15)$$

Since any integer l can be written as $3q \pm 1$ with $q \in \mathbb{Z}$, we

conclude that if $\tilde{\Omega}$ is rational, then the curves must pass for some t through the point $(1/2, 1/2)$, and close to that point the behavior is analogous to the uncorrelated case. In other words, for $\tilde{\Omega}$ rational the order parameter P_C has one branch, among the possibly many, that is equivalent to the function P_U , close to $p = 1/2$.

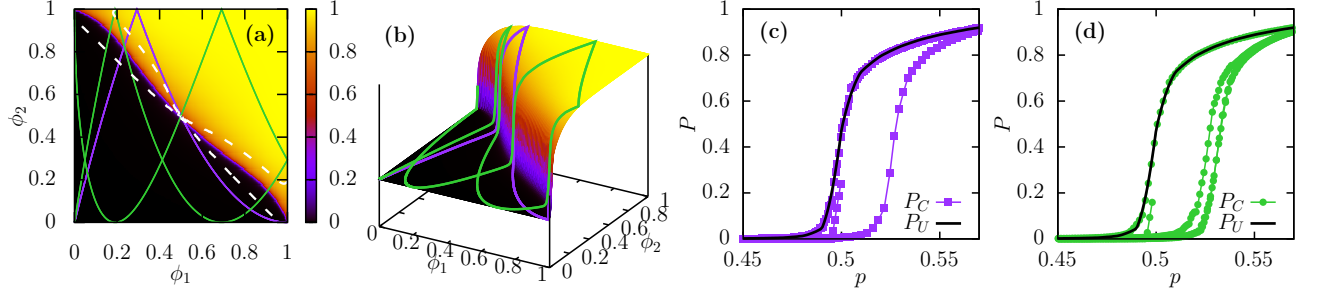


Figure 7. Phase-diagram of two-colour bond percolation on a square lattice. (a) The phase-diagram of S_C in the $\phi_1 - \phi_2$ plane. The continuous lines correspond to a dynamical evolution of ϕ_1 and ϕ_2 as in Eq. (14), for $\tilde{\Omega} = 2$ (purple) and $\tilde{\Omega} = 5/2$ (green). The white dashed lines denote the region where $|S_U - S_C| > 10^{-2}$. (b) 3D plot showing the surface $S(\phi_1, \phi_2)$. Moving on this surface following the violet and green curve we recover $P(t)$. (c) Parametric plot for the order parameter $P_C(p)$ (symbols) and $P_U(p)$ (black line) for $\tilde{\Omega} = 2$ (purple). (d) Same as in (c) but for $\tilde{\Omega} = 5/2$. All numerical simulations are performed on square lattices with $N = 10^6$ nodes, averaged over 100 independent realizations.

Appendix A: Schmidt decomposition

Given an arbitrary state $|\psi\rangle = \sum_{i,j} \Psi_{ij} |i\rangle \otimes |j\rangle$, the Schmidt decomposition [54] tells us that there exist basis of \mathcal{H}_A and \mathcal{H}_B such that

$$|\psi\rangle = \sum_n \sqrt{\alpha_n} |A_n\rangle \otimes |B_n\rangle. \quad (\text{A1})$$

In particular, this is precisely the singular value decomposition of the matrix Ψ [55] formed by the coefficients Ψ_{ij} . Thus the Schmidt coefficients are the square roots of the (real positive) eigenvalues of the matrix $\Psi^\dagger \Psi$. For a system of two qubits this matrix is a 2×2 hermitian, positive definite, matrix, and we can express its eigenvalues in terms of trace and determinant. A straightforward computation gives us

$$\Psi^\dagger \Psi = \begin{bmatrix} |\Psi_{00}|^2 + |\Psi_{10}|^2 & \Psi_{00}^* \Psi_{01} + \Psi_{10}^* \Psi_{11} \\ \Psi_{00} \Psi_{01}^* + \Psi_{10} \Psi_{11}^* & |\Psi_{01}|^2 + |\Psi_{11}|^2 \end{bmatrix}, \quad (\text{A2})$$

from which we get $\text{Tr} \{ \Psi^\dagger \Psi \} = 1$ and

$$\text{Det} \{ \Psi^\dagger \Psi \} = |\det \Psi|^2 = |\Psi_{00}|^2 |\Psi_{11}|^2 + |\Psi_{01}|^2 |\Psi_{10}|^2 - 2\Re \{ \Psi_{00} \Psi_{01}^* \Psi_{10}^* \Psi_{11} \}. \quad (\text{A3})$$

Hence we have

$$\alpha_0 = \frac{1 + \sqrt{1 - 4|\det \Psi|^2}}{2}, \quad (\text{A4})$$

$$\alpha_1 = \frac{1 - \sqrt{1 - 4|\det \Psi|^2}}{2}. \quad (\text{A5})$$

Note that $\alpha_1 = 1 - \alpha_0$, since the trace equals 1, and we need only one Schmidt coefficient that we denote with $\lambda = \alpha_0$. States with $|\text{Det} \{ \Psi \}| = 1/2$ are maximally entangled states, while states with $|\text{Det} \{ \Psi \}| = 0$ are product states.

Appendix B: Average fraction of maximally entangled states

In this section we compute the quantity $p(t)$ given in Eq. (9). Let us assume that the frequencies are random variables following the probability density P_ω . We do not need the frequencies to be independent, we only require that the marginal density is the same for all of them. We can write

$$p(t) = 1 - \mathbb{E} [|\cos(\omega t)|] = 1 - \int_{-\infty}^{+\infty} dx P_\omega(x) |\cos(xt)|. \quad (\text{B1})$$

To compute the integral, we change variable setting $y = xt$, we expand the $|\cos(y)|$ in Fourier series

$$|\cos(y)| = \frac{2}{\pi} - \frac{\pi}{4} \sum_{k=1}^{\infty} \frac{(-1)^k}{4k^2 - 1} \cos(2ky), \quad (\text{B2})$$

and we get

$$\mathbb{E} [|\cos(\omega t)|] = \frac{2}{\pi} - \frac{\pi}{4} \sum_{k=1}^{\infty} \frac{(-1)^k}{4k^2 - 1} \mathbb{E} [\cos(2k\omega t)]. \quad (\text{B3})$$

Writing $\cos(2k\omega t) = \Re [e^{i2k\omega t}]$ we finally get

$$p(t) = 1 - \frac{2}{\pi} + \frac{\pi}{4} \sum_{k=1}^{\infty} \frac{(-1)^k}{4k^2 - 1} \Re [F(2kt)], \quad (\text{B4})$$

where $F(q)$ is the Fourier transform of the probability density P_{ω}

$$F(q) = \mathbb{E} [e^{iq\omega}] = \int dx P_{\omega}(x) e^{iqx}. \quad (\text{B5})$$

The problem of computing $p(t)$ is then reduced to computing the Fourier transform of P_{ω} . In particular, the asymptotic behavior for large t is captured by the asymptotic behavior of $F(q)$ for large q .

1. Gaussian frequencies

For a Gaussian distribution we have $F(q) = e^{-q^2\sigma^2/2}$, thus we get

$$p(t) = 1 - \frac{2}{\pi} + \frac{4}{\pi} \sum_{k=1}^{\infty} \frac{(-1)^k}{4k^2 - 1} \cos(2\Omega kt) e^{-2\sigma^2 t^2 k^2}. \quad (\text{B6})$$

Note that for large t these terms in the series are rapidly suppressed. At leading order we have

$$p(t) \sim 1 - \frac{2}{\pi} - \frac{4}{3\pi} \cos(2\Omega t) e^{-2\sigma^2 t^2}. \quad (\text{B7})$$

The parameters of the Gaussian only come into play in the preasymptotic regime, in particular in the characteristic time $\tau = 1/\sqrt{2\sigma^2}$, while the asymptotic behavior for large t is $p_{\infty} = 1 - 2/\pi$.

2. Discrete distributions: Bernoulli variables

We assume now that ω_e can take values only in a finite set. The simplest scenario we can imagine is a coin tossing: $\omega = \Omega_1$ with probability η and $\omega = \Omega_2$ with probability $1 - \eta$. In this case we have

$$P_{\omega}(x) = \eta\delta(x - \Omega_1) + (1 - \eta)\delta(x - \Omega_2), \quad (\text{B8})$$

where $\delta(x)$ is the Dirac's delta. Setting $\eta = 0$ or $\eta = 1$ we recover the uniform case. Frequencies have expected value $\mathbb{E}[\omega] = \eta\Omega_1 + (1 - \eta)\Omega_2$ and variance $\text{var}[\omega] = \eta(1 - \eta)(\Omega_1 - \Omega_2)^2$. The average fraction of maximally entangled states is given by

$$p(t) = 1 - \eta|\cos(\Omega_1 t)| - (1 - \eta)|\cos(\Omega_2 t)|. \quad (\text{B9})$$

The function $|\cos(\Omega_i t)|$ is periodic with period $T_i = \pi/\Omega_i$. Thus $p(t)$ is periodic with period T if and only if there exist two integers n_1 and n_2 such that $T = n_1 T_1 = n_2 T_2$, which in turn requires $\tilde{\Omega} = \Omega_2/\Omega_1$ to be a rational number. In particular, if $\tilde{\Omega} = l/m$, with l, m coprime integers, then the period is $T = m\pi/\Omega_1$. If instead $\tilde{\Omega}$ is an irrational number, then the function $p(t)$ is quasi-periodic. In both cases, however, the function $P(p)$ is well-defined, indicating that this process is equivalent to uniform bond percolation with probability $p(t)$, as shown in Figure 8.

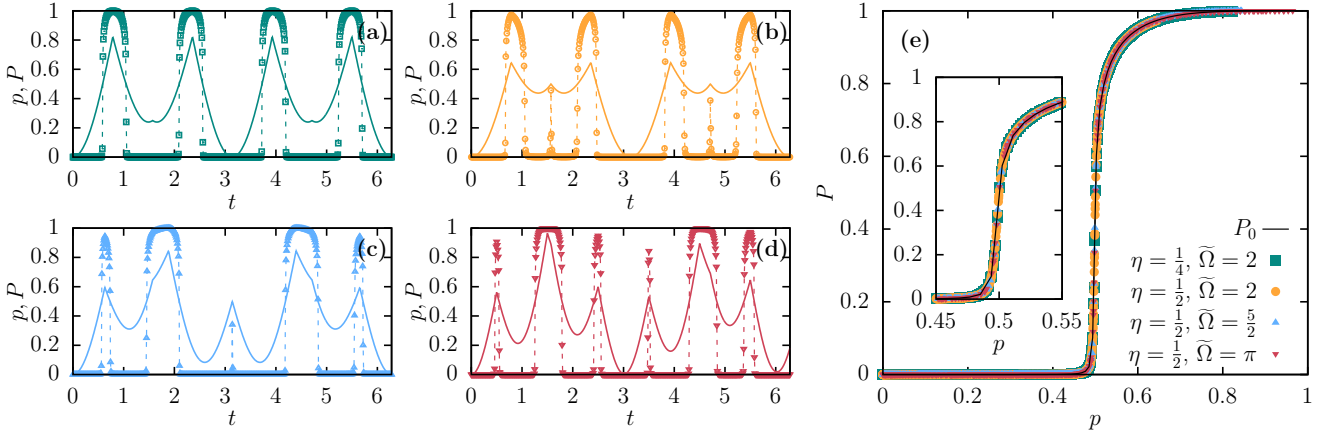


Figure 8. **Dynamical entanglement percolation observables on two-dimensional square lattice with i.i.d. frequencies.** (a)-(d) The observables $p(t)$ (solid lines) and $P(t)$ (symbols and dashed lines) for Bernoulli frequencies, with (a) $\eta = 1/4$, $\tilde{\Omega} = 2$, (b) $\eta = 1/2$, $\tilde{\Omega} = 2$, (c) $\eta = 1/2$, $\tilde{\Omega} = 5/2$, (d) $\eta = 1/2$, $\tilde{\Omega} = \pi$. In (a) and (b) the evolution is periodic with period π ; in (c) the evolution is periodic with period 2π ; in (d) the evolution is quasi-periodic since $\tilde{\Omega}$ is irrational. (e) Parametric plot of $P(p)$ using the observables $p(t)$ and $P(t)$ in panels (a)-(d). As noted for panel (a), the effect of dynamics disappears when observing the order parameter $P(p)$. The inset in panel (e) shows the behavior of $P(p)$ close to the bond percolation threshold $p_c = 1/2$. All data perfectly overlap on the order parameter of uniform bond percolation $P_0(p)$ (black line). For all plots, the system size is $L = 10^3$, hence $N = 10^6$. All results are averaged over 10 realizations of the disorder, and over 100 realizations of the edge activation process.

Appendix C: Distance distribution in a perturbed lattice

In order to characterise the statistical properties of the frequencies, we need to determine P_d , as we can use it to compute P_ω . With no loss of generality, let us take the origin in the unperturbed position of a and rotate the x -axis along the direction of the unperturbed position of b , see for instance nodes $a = 0$ and $a = 2$ in Figure 9(a). In other words, the positions of nodes a and b are $\vec{x}_a = (\delta x_a, \delta y_a)$ and $\vec{x}_b = (1 + \delta x_b, \delta y_b)$, respectively. The difference $\vec{\Delta}_{ab} = \vec{x}_b - \vec{x}_a$ is given by $\vec{\Delta}_{ab} = \vec{\nu} + (\Xi_{ab}, \Theta_{ab})$, where $\vec{\nu} = (1, 0)$ and $\Xi = \delta x_b - \delta x_a$, $\Theta = \delta y_b - \delta y_a \sim \mathcal{N}(0, 2\sigma^2)$, since they are differences of two independent Gaussian random variables with zero mean and variance σ^2 . The modulus of this quantity is the distance between a and b , $d_{ab} = |\vec{\Delta}_{ab}|$, and it follows a Rice distribution [56]

$$\mathcal{R}(x; \nu, \sqrt{2}\sigma) = \frac{x}{2\sigma^2} e^{-\frac{x^2 + \nu^2}{4\sigma^2}} I_0\left(\frac{x\nu}{2\sigma^2}\right), \quad (C1)$$

where $I_0(x)$ is modified Bessel function of the first kind with order zero [57]. Since we are measuring distances in units of lattice spacing, $\nu = 1$, we have

$$P_d(x) = \mathcal{R}(x; 1, \sqrt{2}\sigma). \quad (C2)$$

A change of variable gives us P_ω .

Appendix D: Frequency correlations for the threshold model

As already noted in the main, if frequencies are assigned according to Eq. (12) they are Bernoulli variables with parameter $\eta = \mathbb{P}[d > \lambda]$. Figure 9(a) shows the behavior of this quantity as a function of σ and λ . In particular, for small σ the median is $\lambda \approx 1$ while η rapidly tends to either 1 or 0 away from this line, since d is essentially a Gaussian variable fluctuating around $\mathbb{E}[d]$. In this section we also discuss the correlation between frequencies of adjacent edges.

Imagine three nodes aligned in the unperturbed lattice. To simplify the problem, let us also imagine that, instead of Gaussian perturbations, each point gets shifted to the left or to the right by a fixed amount δ . There are eight equally likely scenarios, corresponding to the various left/right shifts. Among these eight possibilities, in only two the distances are not altered: when the three nodes are all shifted in the same direction. In all remaining six situations, one edge is necessarily shorter than before and the other is longer. Thus we expect, from this naive argument, that the distances along the same direction should be anti-correlated. We can quantify this intuition, and carry out

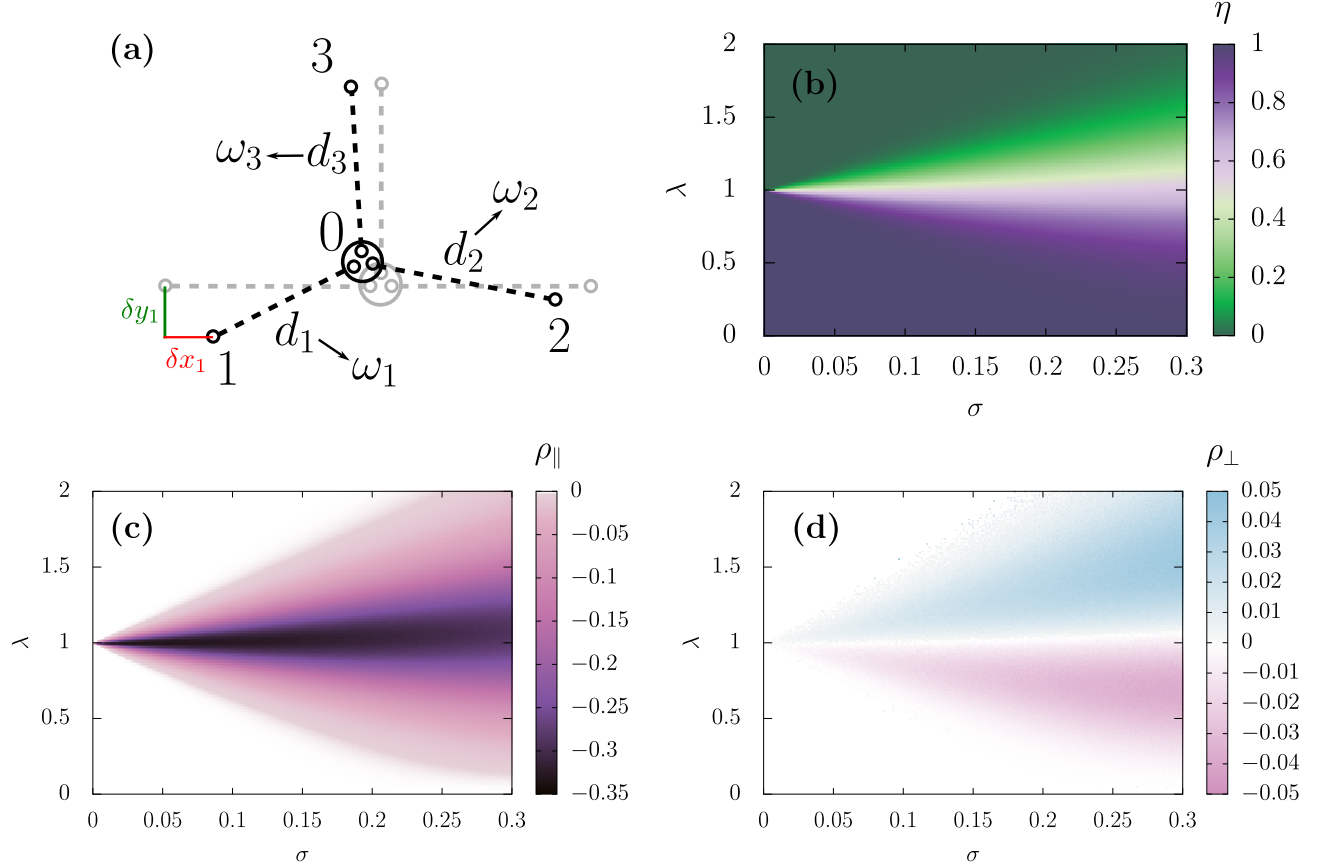


Figure 9. Spatial correlations in the perturbed lattice. (a) Four nodes in the perturbed lattice. Original unperturbed lattice positions are represented with lighter gray lines. For the sake of simplicity, we only represented one qubit on stations 1, 2, and 3. The position of each point is shifted by the independent Gaussian variables δx and δy (see for instance red and green lines for qubit 1). Edges (1,0) and (0,2) are said to be collinear, while (1,0) and (0,3) are perpendicular. (b) Numerical evaluation of the probability $\eta(\sigma, \lambda)$. The white line corresponds to the median of the distribution, i.e., where $\eta = 1/2$. Numerical evaluation of (c) ρ_{\parallel} and (d) ρ_{\perp} for the two-frequency system, as a function of the noise strength σ and the threshold distance λ . Collinear frequencies are anti-correlated, correlations being stronger for $\lambda \approx 1$. Correlations between perpendicular frequencies are instead much weaker. Each point is averaged over 10^6 random realizations of the scenario described in panel (a).

computations explicitly under a small noise assumption. Let us consider three nodes (1, 0 and 2) which are three collinear neighbors, and another node (3) that is neighbor of node 0 along the orthogonal direction, see Figure 9(a). With no loss of generality let us place 0 in the origin. We then have for the distances

$$d_1 = d_{10} = \sqrt{(1 + \Xi_{10})^2 + \Theta_{10}^2} \approx 1 + \Xi_{10}, \quad (\text{D1})$$

$$d_2 = d_{20} = \sqrt{(1 - \Xi_{20})^2 + \Theta_{20}^2} \approx 1 - \Xi_{20}, \quad (\text{D2})$$

$$d_3 = d_{30} = \sqrt{\Xi_{30}^2 + (\Theta_{30} + 1)^2} \approx 1 + \Theta_{30}. \quad (\text{D3})$$

Since Ξ_{10} and Ξ_{20} are correlated while Ξ_{10} and Θ_{30} are uncorrelated, it follows that $\text{cov}(d_1, d_2) \approx -\sigma^2$, and $\text{cov}(d_1, d_3) \approx 0$, at lowest order in σ . Thus for low noise we have indeed anti-correlation for the lengths of collinear edges, and no correlations for the lengths of perpendicular edges.

To quantify the amount of correlations, we introduce the joint probability densities $P_{d_1, d_2 \parallel}(x_1, x_2)$ and $P_{d_1, d_2 \perp}(x_1, x_2)$ for the lengths of two adjacent collinear and perpendicular edges, respectively. From these densities, we can compute the joint distributions of the frequencies $P_{\omega_1, \omega_2 \parallel}(x_1, x_2)$ and $P_{\omega_1, \omega_2 \perp}(x_1, x_2)$, using a simplified notation where ω_i denotes the frequency of the edge of length d_i , as in Figure 9, and the Pearson's coefficients

$$\rho_X = \frac{\text{cov}(\omega_1, \omega_2 | X)}{\text{var}[\omega]} = \frac{\int \int dx_1 dx_2 P_{\omega_1, \omega_2 | X}(x_1, x_2) x_1 x_2 - \mathbb{E}[\omega]^2}{\int dx P_{\omega}(x) x^2 - \mathbb{E}[\omega]^2} = \frac{\mathbb{E}[\omega_1 \omega_2 | X] - \mathbb{E}[\omega]^2}{\mathbb{E}[\omega^2] - \mathbb{E}[\omega]^2}, \quad (\text{D4})$$

with $X = \parallel$ for the collinear case, and $X = \perp$ for the perpendicular case, see Figure 9(a). As already pointed out, no analytical expression can be found for these joint densities, and we need to resort to numerical methods. However, for the two-frequencies case everything turns out to be much simplified, as only three parameters are needed to completely characterize correlations. Since the value of the frequency ω depends on whether $d > \lambda$ or not, for the two frequencies of adjacent edges – note that there is no need to distinguish between collinear and perpendicular at this stage – we can have: (i) both $\omega_1 = 1$ and $\omega_2 = 1$, which happens if both $d_1 < \lambda$ and $d_2 < \lambda$ thus with probability $\mathbb{P}_{>,>} = \mathbb{P}[d_1 > \lambda, d_2 > \lambda]$; (ii) $\omega_1 = 1$ and $\omega_2 = \Omega$, with probability $\mathbb{P}_{>,<}$; (iii) $\omega_1 = \Omega$ and $\omega_2 = 1$, with probability $\mathbb{P}_{<,>}$; (iv) both $\omega_1 = \omega_2 = \Omega$, with probability $\mathbb{P}_{<,<}$. In summary, we have

$$P_{\omega_1, \omega_2}(x_1, x_2) = \mathbb{P}_{>,>} \delta(x_1 - 1) \delta(x_2 - 1) + \mathbb{P}_{>,<} \delta(x_1 - 1) \delta(x_2 - \Omega) + \mathbb{P}_{<,>} \delta(x_1 - \Omega) \delta(x_2 - 1) + \mathbb{P}_{<,<} \delta(x_1 - \Omega) \delta(x_2 - \Omega). \quad (\text{D5})$$

By normalization, these four probabilities must sum up to 1. Furthermore, by symmetry $\mathbb{P}_{<,>} = \mathbb{P}_{>,<}$. Finally, note that $\mathbb{P}_{>,<} + \mathbb{P}_{<,>} = \eta$, as we have integrated out over the variable d_2 and we are left with the marginal on d_1 . Calling $\beta = \mathbb{P}_{<,<}$, we need only the parameters η and β to characterize the joint distribution and thus the correlations. Note that the geometric constraint of considering collinear rather than perpendicular edges enters in the explicit evaluation of β . When we need to specify which case we are dealing with, we denote with β_{\parallel} and β_{\perp} the collinear and perpendicular cases, respectively. Since we have $\mathbb{P}_{<,<} = \beta$, $\mathbb{P}_{<,>} = \mathbb{P}_{>,<} = 1 - \eta - \beta$, and $\mathbb{P}_{>,>} = \beta + \eta - (1 - \eta)$, we can compute

$$\mathbb{E}[\omega_1 \omega_2] = \mathbb{P}_{>,>} + 2\Omega \mathbb{P}_{<,>} + \Omega^2 \mathbb{P}_{<,<} = \beta(\Omega - 1)^2 + \eta - (1 - \eta) + 2(1 - \eta)\Omega, \quad (\text{D6})$$

and, subtracting $\mathbb{E}[\omega^2] = \eta + (1 - \eta)\Omega^2$, we get

$$\text{cov}(\omega_1, \omega_2) = (\Omega - 1)^2[\beta - (1 - \eta)^2]. \quad (\text{D7})$$

If $\Omega \neq 1$ – otherwise $\text{cov}(\omega_1, \omega_2) = \text{var}[\omega] = 0$ – we obtain from Eq. (D4)

$$\rho_X = \frac{\beta_X - (1 - \eta)^2}{\eta(1 - \eta)}. \quad (\text{D8})$$

Note that this expression does not depend on Ω . It is just a measure of the tendency of two adjacent frequencies to be similar. If there are no spatial constraints, we have $\beta_X = (1 - \eta)^2$ and $\rho_X = 0$. However, as we have already noted, we expect collinear distances to be negatively correlated, implying that $\beta_{\parallel} < (1 - \eta)^2$. Thus we expect $\rho_{\parallel} \leq 0$. On the other hand, weak correlations appear for perpendicular distances, at least in the small noise limit. This is confirmed by means of numerical evaluation of ρ_X , as reported in Figure 9(c)-(d), obtained averaging over 10^6 random realizations of the four-node scenario described in 9(a). Alternatively, one can compute η using the Gaussian small-noise approximation of the Rice distribution [57], and β by Monte Carlo integration.

Appendix E: Mean-field solution for the two-colour bond percolation

The basic idea to derive a mean-field solution for a percolation process is to consider the process on a random network, ignore the presence of short loops and use the formalism of branching processes [58]. To model the case of square lattice, we consider a random regular graph with coordination number $k = 4$, and each node has attached exactly two edges of each type. This graph model is a particular case of a more general coloured configuration model [50]. Let us denote by m_1 the probability that if we follow an active edge of type 1 we reach the GC. m_2 is defined analogously. An active edge leads to the GC if at least one of the outgoing edges leads to the GC. Ignoring the presence of loops we can assume that edge probabilities are independent – and here lies the tree-like approximation. Thus we can write

$$m_1 = 1 - (1 - \phi_1 m_1)(1 - \phi_2 m_2)^2, \quad (\text{E1})$$

$$m_2 = 1 - (1 - \phi_1 m_1)^2(1 - \phi_2 m_2). \quad (\text{E2})$$

The stable fixed point of these equations (m_1^*, m_2^*) gives us the probability that following a random link we reach the GC. A similar argument allows us to get an equation for the size of the GC. One node is in the GC if at least one of its edges leads to it, and this occurs with probability

$$S = 1 - (1 - \phi_1 m_1^*)^2(1 - \phi_2 m_2^*)^2. \quad (\text{E3})$$

Thus the stable fixed point of Eqs. (E1) and (E2) plugged into the expression for S gives us the order parameter $S(\phi_1, \phi_2)$.

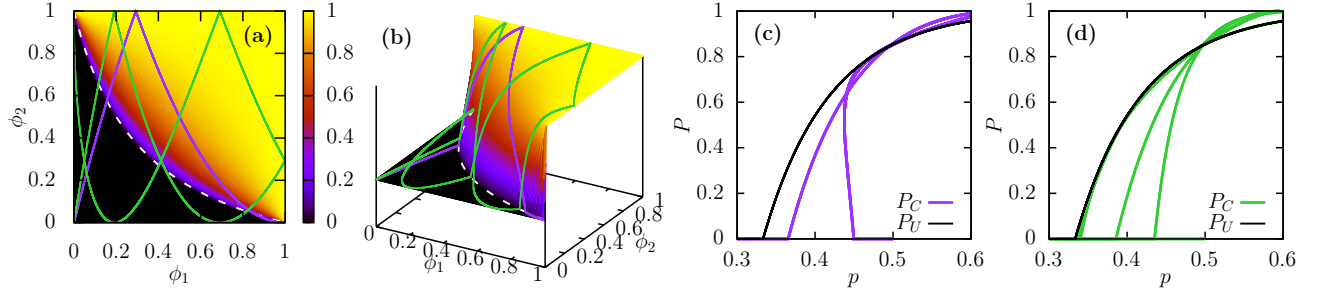


Figure 10. Mean-field phase diagram for the two-colour bond percolation. (a) The phase diagram in the parameter plane $\phi_1 - \phi_2$. The dashed line corresponds to the critical threshold Eq. (E5), the continuous lines are two dynamical evolutions as in Eq. (14) with $\tilde{\Omega} = 2$ (purple) and $\tilde{\Omega} = 5/2$ (green). Arrows indicate the direction of time up to half of the period. (b) 3D plot of the surface $S(\phi_1, \phi_2)$. Lines are the evolution of S along the curves in panel (a). (c)-(d) Time evolution of $p(t)$ (dashed lines) and $P(t) = S(\phi_1(t), \phi_2(t))$ (continuous lines) for (c) $\tilde{\Omega} = 2$ and (d) $\tilde{\Omega} = 5/2$. (e) Plot of $P(p)$ for $\tilde{\Omega} = 2$ (purple) and $\tilde{\Omega} = 5/2$ (green). Black dotted lines indicate the position of the uniform percolation threshold $p_c = 1/3$. (e) The order parameter $P(p)$ obtained from a parametric plot of the observables P and t in panels (c)-(d). The black line is the order parameter of uniform bond percolation. The overall picture is qualitatively analogous to what we observe in numerical simulations in two-dimensional lattices, Figure 7.

1. Percolation threshold

Note that $m_1^* = m_2^* = 0$ is always a trivial solution of the fixed-point equations, and it corresponds to $S = 0$, i.e., no GC exists. However, for $\phi_1 = \phi_2 = 1$ we have another solution $m_1 = m_2 = 1$. Thus there must exist a critical value of the parameters ϕ_1, ϕ_2 separating a phase with no GC from a phase with a GC. This defines a percolation line. We can determine such a critical line studying the stability of the trivial fixed point to determine where another stable solution with positive probabilities appear. The largest eigenvalue of the Jacobian matrix, of Eqs. (E1)-(E2), evaluated in $(0, 0)$, is given by

$$\Lambda(\phi_1, \phi_2) = \frac{\phi_1 + \phi_2 + \sqrt{\phi_1^2 + \phi_2^2 + 14\phi_1\phi_2}}{2}. \quad (\text{E4})$$

The trivial fixed point $(0, 0)$ remains stable until $\Lambda = 1$. This condition defines a critical line in the $\phi_1 - \phi_2$ plane determined by the equation

$$3\phi_1\phi_2 - \phi_1 - \phi_2 + 1 = 0, \quad (\text{E5})$$

see the dashed line in Figure 10(a) which separates a phase with no GC (below) from a phase with a GC (above).

2. Dynamical evolution for the activation probabilities

As shown in the main, the case of activation probabilities that evolve in time is described by a curve $(\phi_1(t), \phi_2(t))$ in the parameter space, see the continuous lines in Figure 10(a). Thus, the order parameter $P(t)$ is obtained as $P(t) = S(\phi_1(t), \phi_2(t))$. Clearly, the local constraint in the problem result in an order parameter that cannot be expressed in terms of the fraction of active edges p .

3. Random reshuffling

Using the analytical mean-field solution, we can analyze what happens if we perform a random rewiring of the edges, destroying the correlation structure. In such a case, we have a global constraints setting half of the edges per type. Thus there is no local constraint on the edges attached on each node. In other words, each edge is either of type 1 or 2 with probability $1/2$, independently from the neighbors. Thus Eq. (E1) and Eq. (E2) denote the probability of one particular configuration of the possible realizations of a node's neighborhood. Averaging over all possible configurations we get

$$m_1 = 1 - \frac{1}{2^3} \sum_{n=0}^3 \binom{3}{n} (1 - \phi_1 m_1)^n (1 - \phi_2 m_2)^{3-n} = 1 - \left(1 - \frac{\phi_1 m_1 + \phi_2 m_2}{2}\right)^3, \quad (\text{E6})$$

and correspondingly for m_2 . Since it follows that $m_1 = m_2 = m$, the branching process can be solved using just one recursive equation

$$m = 1 - (1 - pm)^3, \quad (\text{E7})$$

where $p = (\phi_1 + \phi_2)/2$ is the average fraction of active edges. The same argument leads to an equation for the order parameter

$$P_U = 1 - (1 - pm)^4. \quad (\text{E8})$$

These two last equations are the well-known solution for uniform bond percolation on a random regular graph with activation probability p . This shows explicitly that the role of the microscopic disorder disappears as soon as edge correlations are removed.

[1] A. K. Ekert, Quantum cryptography based on bell's theorem, *Phys. Rev. Lett.* **67**, 661 (1991).

[2] R. Raussendorf, D. E. Browne, and H. J. Briegel, Measurement-based quantum computation on cluster states, *Phys. Rev. A* **68**, 022312 (2003).

[3] R. Van Meter, K. Nemoto, and W. Munro, Communication links for distributed quantum computation, *IEEE Transactions on Computers* **56**, 1643 (2007).

[4] S. Wehner, D. Elkouss, and R. Hanson, Quantum internet: A vision for the road ahead, *Science* **362**, eaam9288 (2018).

[5] K. Azuma, S. Bäuml, T. Coopmans, D. Elkouss, and B. Li, Tools for quantum network design, *AVS Quantum Science* **3**, 014101 (2021).

[6] L. Cirigliano, V. Brosco, C. Castellano, C. Conti, and L. Pilozzi, Optimal quantum key distribution networks: capacitance versus security, *Npj Quantum Inf.* **10**, 44 (2024).

[7] T. P. Spiller, K. Nemoto, S. L. Braunstein, W. J. Munro, P. v. Loock, and G. J. Milburn, Quantum computation by communication, *New Journal of Physics* **8**, 30 (2006).

[8] R. Van Meter and S. J. Devitt, The path to scalable distributed quantum computing, *Computer* **49**, 31 (2016).

[9] P. Kómár, E. M. Kessler, M. Bishop, L. Jiang, A. S. Sørensen, J. Ye, and M. D. Lukin, A quantum network of clocks, *Nature Physics* **10**, 582 (2014).

[10] W. McKenzie, A. M. Richards, S. Patel, T. Gerrits, T. Akin, S. Peil, A. T. Black, D. Tulchinsky, A. Hastings, Y.-S. Li-Baboud, *et al.*, Clock synchronization characterization of the washington dc metropolitan quantum network (dc-qnet), *Applied Physics Letters* **125**, 10.1063/5.0225082 (2024).

[11] J. Tura, R. Augusiak, A. B. Sainz, T. Vértesi, M. Lewenstein, and A. Acín, Detecting nonlocality in many-body quantum states, *Science* **344**, 1256 (2014).

[12] J. Biamonte, M. Faccin, and M. De Domenico, Complex networks from classical to quantum, *Communications Physics* **2**, 10.1038/s42005-019-0152-6 (2019).

[13] A. Osterloh, L. Amico, G. Falci, and R. Fazio, Scaling of entanglement close to a quantum phase transition, *Nature* **416**, 608 (2002).

[14] G. Bianconi, Superconductor-insulator transition in a network of 2d percolation clusters, *EPL (Europhysics Letters)* **101**, 26003 (2013).

[15] M. Walschaers, B. Sundar, N. Treps, L. D. Carr, and V. Parigi, Emergent complex quantum networks in continuous-variables non-gaussian states, *Quantum Science and Technology* **8**, 035009 (2023).

[16] T. Mendes-Santos, M. Schmitt, A. Angelone, A. Rodriguez, P. Scholl, H. J. Williams, D. Barredo, T. Lahey, A. Browaeys, M. Heyl, and M. Dalmonte, Wavefunction network description and kolmogorov complexity of quantum many-body systems, *Phys. Rev. X* **14**, 021029 (2024).

[17] G. Bellomia, C. Mejuto-Zaera, M. Capone, and A. Amaretti, Quasilocal entanglement across the mott-hubbard transition, *Phys. Rev. B* **109**, 115104 (2024).

[18] D. Cavalcanti, M. L. Almeida, V. Scarani, and A. Acín, Quantum networks reveal quantum nonlocality, *Nature communications* **2**, 184 (2011).

[19] D. S. Bhakuni, R. Verdel, C. Muzzi, R. Andreoni, M. Aidelsburger, and M. Dalmonte, Diagnosing quantum transport from wave function snapshots, *Physical Review B* **110**, 144204 (2024).

[20] R. Andreoni, V. Vitale, C. Muzzi, G. Caldarelli, R. Verdel, and M. Dalmonte, Network theory classification of quantum matter based on wave function snapshots (2025), arXiv:2512.02121 [quant-ph].

[21] R. Albert and A.-L. Barabási, Statistical mechanics of complex networks, *Reviews of Modern Physics* **74**, 47 (2002).

[22] N. Brunner, D. Cavalcanti, S. Pironio, V. Scarani, and S. Wehner, Bell nonlocality, *Reviews of Modern Physics* **86**, 419 (2014).

[23] S. Das, S. Khatri, and J. P. Dowling, Robust quantum network architectures and topologies for entanglement distribution, *Physical Review A* **97**, 012335 (2018).

[24] G. Adesso, T. R. Bromley, and M. Cianciaruso, Measures and applications of quantum correlations, *Journal of Physics A: Mathematical and Theoretical* **49**, 473001 (2016).

[25] A. Streltsov, G. Adesso, and M. B. Plenio, Colloquium: Quantum coherence as a resource, *Reviews of Modern Physics* **89**, 041003 (2017).

[26] H. Shimizu, W. Roga, D. Elkouss, and M. Takeoka, Simple loss-tolerant protocol for greenberger-horne-zeilinger-state distribution in a quantum network, *Physical Review A* **111**, 022624 (2025).

[27] M. Płodzień, M. Lewenstein, and J. Chwedeńczuk, Many-body quantum resources of graph states, *Reports on Progress in Physics* **88**, 077601 (2025).

- [28] K. Kieling, T. Rudolph, and J. Eisert, Percolation, renormalization, and quantum computing with nondeterministic gates, *Physical Review Letters* **99**, 130501 (2007).
- [29] A. Acín, J. I. Cirac, and M. Lewenstein, Entanglement percolation in quantum networks, *Nature Physics* **3**, 256 (2007).
- [30] D. E. Browne, M. B. Elliott, S. T. Flammia, S. T. Merkel, A. Miyake, and A. J. Short, Phase transition of computational power in the resource states for one-way quantum computation, *New Journal of Physics* **10**, 023010 (2008).
- [31] M. Cuquet and J. Calsamiglia, Entanglement percolation in quantum complex networks, *Physical Review Letters* **103**, 240503 (2009).
- [32] S. Perseguers, M. Lewenstein, A. Acín, and J. I. Cirac, Quantum random networks, *Nature Physics* **6**, 539 (2010).
- [33] M. Cuquet and J. Calsamiglia, Limited-path-length entanglement percolation in quantum complex networks, *Physical Review A* **83**, 032319 (2011).
- [34] S. Perseguers, G. J. Lapeyre, D. Cavalcanti, M. Lewenstein, and A. Acín, Distribution of entanglement in large-scale quantum networks, *Reports on Progress in Physics* **76**, 096001 (2013).
- [35] D. Stauffer and A. Aharony, *Introduction to Percolation Theory* (CRC press, 2018).
- [36] M. Kim and F. Radicchi, Shortest-path percolation on random networks, *Phys. Rev. Lett.* **133**, 047402 (2024).
- [37] X. Meng, B. Hao, B. Ráth, and I. A. Kovács, Path percolation in quantum communication networks, *Phys. Rev. Lett.* **134**, 030803 (2025).
- [38] A. De Girolamo, G. Magnifico, and C. Lupo, Percolation thresholds and connectivity in quantum networks, *Quantum Science and Technology* **10**, 035047 (2025).
- [39] Y. Hu *et al.*, Unveiling the importance of nonshortest paths in quantum networks, *Sci. Adv.* **11**, eadt2404 (2025).
- [40] X. Yang, Y.-H. Yang, and M.-X. Luo, Strong entanglement distribution of quantum networks, *Phys. Rev. Res.* **4**, 013153 (2022).
- [41] S. Brito, A. Canabarro, R. Chaves, and D. Cavalcanti, Statistical properties of the quantum internet, *Phys. Rev. Lett.* **124**, 210501 (2020).
- [42] X. Meng, N. L. Piparo, K. Nemoto, and I. A. Kovács, Quantum communication networks enhanced by distributed quantum memories, *Quantum* **9**, 1948 (2025).
- [43] G. D. Chiara, S. Montangero, P. Calabrese, and R. Fazio, Entanglement entropy dynamics of Heisenberg chains, *Journal of Statistical Mechanics: Theory and Experiment* **2006**, P03001 (2006).
- [44] H. Kim and D. A. Huse, Ballistic Spreading of Entanglement in a Diffusive Nonintegrable System, *Physical Review Letters* **111**, 127205 (2013).
- [45] J. Eisert, M. Friesdorf, and C. Gogolin, Quantum many-body systems out of equilibrium, *Nature Physics* **11**, 124 (2015).
- [46] N. Laflorencie, Quantum entanglement in condensed matter systems, *Physics Reports* **646**, 1 (2016).
- [47] M. Hoshino, M. Oshikawa, and Y. Ashida, Entanglement swapping in critical quantum spin chains, *Physical Review B* **111**, 155143 (2025).
- [48] J. T. Chayes, L. Chayes, and R. Durrett, Inhomogeneous percolation problems and incipient infinite clusters, *Journal of Physics A: Mathematical and General* **20**, 1521 (1987).
- [49] Y. Zhang, A Note on Inhomogeneous Percolation, *The Annals of Probability* **22**, 803 (1994).
- [50] I. Kryven, Bond percolation in coloured and multiplex networks, *Nature communications* **10**, 404 (2019).
- [51] G. Vidal, Entanglement of pure states for a single copy, *Phys. Rev. Lett.* **83**, 1046 (1999).
- [52] C. R. Scullard and R. M. Ziff, Critical surfaces for general inhomogeneous bond percolation problems, *Journal of Statistical Mechanics: Theory and Experiment* **2010**, P03021 (2010).
- [53] L. Cirigliano, Dynamical entanglement percolation with spatially correlated disorder, <https://github.com/lorenzocirigliano> (2026).
- [54] M. A. Nielsen and I. L. Chuang, *Quantum Computation and Quantum Information: 10th Anniversary Edition* (Cambridge University Press, 2010).
- [55] R. A. Horn and C. R. Johnson, *Matrix Analysis* (Cambridge University Press, 2012).
- [56] S. O. Rice, Mathematical analysis of random noise, *The Bell System Technical Journal* **23**, 282 (1944).
- [57] M. Abramowitz and I. A. Stegun, *Handbook of mathematical functions: with formulas, graphs, and mathematical tables*, Vol. 55 (Courier Corporation, 1965).
- [58] S. N. Dorogovtsev and J. F. F. Mendes, *The Nature of Complex Networks* (Oxford University Press, 2022).